# Flow topology of rare back flow events and critical points in turbulent channels and toroidal pipes

IOP Conf. Series: Journal of Physics: Conf. Series **1001** (2018) 012002 doi:10.1088/1742-6596/1001/1/012002

# Flow topology of rare back flow events and critical points in turbulent channels and toroidal pipes

**C. Chin[1], R. Vinuesa[2], R. Örlü[2], J. I. Cardesa[3], A. Noorani[2], P. Schlatter[2] and M. S. Chong[4]**

[1]School of Mechanical Engineering, University of Adelaide, South Australia 5005, Australia
[2]Linné FLOW Centre, KTH Mechanics, SE-100 44 Stockholm, Sweden
[3]School of Aeronautics, Universidad Politécnica de Madrid, Madrid, Spain
[4]Mechanical Engineering Department, University of Melbourne, Victoria 3010, Australia

E-mail: rey.chin@adelaide.edu.au

**Abstract.** A study of the back flow events and critical points in the flow through a toroidal pipe at friction Reynolds number $Re_\tau \approx 650$ is performed and compared with the results in a turbulent channel flow at $Re_\tau \approx 934$. The statistics and topological properties of the back flow events are analysed and discussed. Conditionally-averaged flow fields in the vicinity of the back flow event are obtained, and the results for the torus show a similar streamwise wall-shear stress topology which varies considerably for the spanwise wall-shear stress when compared to the channel flow. The comparison between the toroidal pipe and channel flows also shows fewer back flow events and critical points in the torus. This cannot be solely attributed to differences in Reynolds number, but is a clear effect of the secondary flow present in the toroidal pipe. A possible mechanism is the effect of the secondary flow present in the torus, which convects momentum from the inner to the outer bend through the core of the pipe, and back from the outer to the inner bend through the pipe walls. In the region around the critical points, the skin-friction streamlines and vorticity lines exhibit similar flow characteristics with a node and saddle pair for both flows. These results indicate that back flow events and critical points are genuine features of wall-bounded turbulence, and are not artifacts of specific boundary or inflow conditions in simulations and/or measurement uncertainties in experiments.

## 1. Introduction

A detailed assessment of the near-wall region in turbulent flows is a very complex problem, which involves a number of interesting fundamental questions including its modulation by the flow in the outer region [1, 2, 3, 4]. The transport phenomena [5] present close to the wall, which can be characterised in terms of the wall-shear stress vector field, are relevant to understand a wide range of applications, including cardiovascular flows [6] (and also as discussed by Arzani *et al.* [7] in the context of Lagrangian wall-shear stress structures) and heat transfer (see for instance the studies by Dairay *et al.* [8] and Wu *et al.* [9]). In particular, the presence of regions of instantaneous reverse flow (denoted in the present work as back flow events) in wall-bounded turbulence is a topic of relevance for the understanding of separation mechanisms, both in steady [10] and unsteady [11] aerodynamic applications. A recent review by Carlomagno & Ianiro [12] discussed that flow reversal produced by local pressure gradient fluctuations in the near-wall can initiate secondary vortices. It is reported that this flow reversal is one of two features (the other being vortex generation) that can enhance the heat transfer characteristics

in the flow. Moreover, back flow events and the topology of the wall-shear stress have been used to further understand the separation mechanisms from the perspective of dynamical systems [13], control theory [14] and reduced-order modelling [15], among others. Back flow events in turbulent channel flow were characterised in detail by Lenaers *et al.* [16], together with extreme wall-normal velocity fluctuations near the wall. In their direct numerical simulations (DNSs), they found that both the probability of finding a back flow event and the distance from the wall at which reverse flow was observed increased with Reynolds number. These indications show that there is a connection between the modulation of the near-wall region by the large-scale motions in the outer part of the flow and the presence of back flow events. This connection was quantitatively investigated by documenting the back-flow event density beneath large-scale structures residing in the logarithmic layer. Their conclusions were confirmed in a DNS of turbulent channel flow [17] at a slightly higher Reynolds number, where a probability of finding back flow events of around 0.07% was reported at a friction Reynolds number of $Re_\tau = 2,000$. Note that $Re_\tau$ is formed in terms of the channel half-height $h$, the friction velocity $u_\tau = \sqrt{\tau_w/\rho}$ (where $\tau_w$ is the wall-shear stress and $\rho$ is the fluid density) and the kinematic viscosity $\nu$ of the fluid. In both studies a strong connection between the presence of back flow events and energetic large-scale motions in the outer region were reported. These studies confirmed the indications in earlier works [18, 19, 20] regarding the presence of back flow events in wall-bounded turbulence, despite the fact that they had not been identified in certain measurement campaigns [21, 22]. The more recent experimental study by Willert [23], who performed particle image velocimetry (PIV) measurements in zero-pressure-gradient (ZPG) turbulent boundary layers (TBLs) at $Re_\tau = 1,000$ and $2,700$, confirmed the findings by Lenaers *et al.* [16] and Yao *et al.* [17]. Brücker [24] used micro-pillar sensors to measure the topology of the wall-shear stress vector in a ZPG TBL at $Re_\tau \simeq 940$, and identified a probability of finding back flow events of around 0.05%, aligned with the results by Lenaers *et al.* [16] at approximately the same $Re$. Note that micro-pillar sensors, based on correlating the deflection of small flexible pillars on the wall and the shear stress, provide accurate measurements of the $\tau_w$ fluctuations, as well as their spatial correlations (see Refs. [25, 26, 27]). Thus, Brücker [24] was able to determine that back flow events are correlated with strong spanwise gradients of the wall-shear stress, and characterised the topology of critical points (defined as points where both the wall-shear stress and the surface vorticity are zero), which are correlated with large-scale events in the logarithmic layer. This correlation was investigated by Monty *et al.* [28], Chong *et al.* [29] and Cardesa *et al.* [30] using DNS of turbulent channel and pipe flows, and they reported that critical points are formed when large-scale motions transport vorticity towards the wall.

Extreme events close to the wall have been mostly studied in canonical cases, such as turbulent channel flows and ZPG TBLs. The effect of an adverse pressure gradient (APG) was studied by Vinuesa *et al.* [31] using a DNS of the flow around a NACA4412 wing section [10]. In that study it is reported that the APG increases the probability of finding back flow events as the Clauser pressure-gradient parameter $\beta = \delta^*/\tau_w \mathrm{d}P/\mathrm{d}x$ (note that $\delta^*$ is the displacement thickness and $\mathrm{d}P/\mathrm{d}x$ is the streamwise pressure gradient) increases. The APG reduces the velocity gradient at the wall, and produces more energetic large-scale motions in the outer region [32]. Thus, the combination of both effects leads to the increase of back flow events. Their analysis of extreme events also revealed that under very strong APG conditions (*i.e.*, values of $\beta \simeq 35$), the flow is either aligned with the stream or against it, with a reduced spanwise wall-shear component, which is otherwise large at lower values of $\beta$. The characteristics of back flow events in APG TBLs were studied experimentally by Bross and Kähler [33] using time-resolved tomographic PIV measurements, which allowed them to characterise the flow structure around the regions of reverse flow.

Note that periodic boundary conditions were imposed in the spanwise direction (as well as in the streamwise direction in the case of channel flow) in all the simulations discussed above.

Although the existence of back flow events has been established beyond doubt, a perfect flow case to study back flow events would be one in which the imposed periodicity is not only part of the computational setup, but a feature of the flow case itself. Such a geometry and flow case is given by the flow through a toroidal pipe. The relevance of this flow case is related to the fact that it serves as the common asymptotic limit of two distinct classes of important flow cases, *i.e.*, the flow in spatially-developing pipe bends (when entry effects become negligible), and the flow in helical pipes (when the torsion becomes negligible). Since the experimental realisation of the flow through a toroidal pipe is complicated [34], their stability [35] as well as laminar [36] and turbulent [37] base flows (covering a wide range of curvatures) have only recently been explored by means of DNS.

In the present study we analyse the characteristics of back flow events in toroidal pipes using a numerical approach similar to the one reported in Ref. [38], in order to exploit the naturally-occurring periodicity in the flow to address the question of back flow events and critical points. In incompressible wall-bounded flows, the skin-friction and surface-vorticity fields are associated with turbulence transport mechanisms [39, 40]. Besides the physical nature of the periodicity in the torus, flows through curved pipes are characterised by a strong in-plane secondary flow that has a strong impact on the kinematics and dynamics of the flow [41], which makes it an interesting flow case with respect to back flow events and critical points.

## 2. Method

### *2.1. Channel flow simulations*

The turbulent channel flow data used for the present study comes from a direct numerical simulation (DNS). The numerical scheme integrates the fluid flow equations following the method described in Ref. [42]. On the wall-parallel planes, space is discretised using Fourier expansions, while Chebyshev polynomials are used in the wall-normal direction. The data set used here is a smaller version of case L950 in Ref. [43], and the details of the present simulation are summarised in table 1. The mesh resolutions in the streamwise and spanwise directions are denoted by $\Delta_x$ and $\Delta_z$, respectively, and the corresponding lengths of the computational domain are $L_x$ and $L_z$. The streamwise computational domain length is $L_x = 2\pi\delta$. The effects of insufficient computational length are well documented [39, 44] (*e.g.* lack of convergence of higher-order turbulence statistics). However, it is shown that statistics at the near wall with the current domain length $L_x = 2\pi\delta$ remain unaffected [45, 46]. The number of coefficients in the Fourier expansions in those two directions are $N_x = 512$ and $N_z = 511$, whereas $N_y = 385$ denotes the number of Chebyshev polynomials of the wall-normal direction. The superscript '+' is used to denote viscous scaling, *i.e.* in terms of the friction velocity $u_\tau$ or the viscous length $\nu/u_\tau$.

### *2.2. Simulation of the flow through a toroidal pipe*

The DNS of the turbulent flow through a toroidal pipe was performed using the numerical code Nek5000, developed at the Argonne National Laboratory by Fischer *et al.* [47] and based on the spectral-element method (SEM) by Patera [48]. Lagrange interpolants of order $N$ are used to expand the velocity and pressure, respectively, at the Gauss–Lobatto–Legendre (GLL) quadrature points within the spectral elements. The nonlinear terms in the incompressible Navier–Stokes equations are treated explicitly through third-order extrapolation (EXT3), and an implicit third-order backward differentiation (BDF3) scheme is used for the viscous terms. Numerical stability of the SEM was ensured through explicit filtering of 5% of the energy of the highest mode (see the work by Fischer and Mullen [49] for additional details). The simulations were carried out on the Cray XC40 system "Beskow", located at the PDC Center from KTH, running on 4,096 cores.

The toroidal pipe under consideration is shown in figure 1, which is similar to the bent pipes considered by Noorani *et al.* [37]. Figure 1(a) shows the instantaneous streamwise wall-

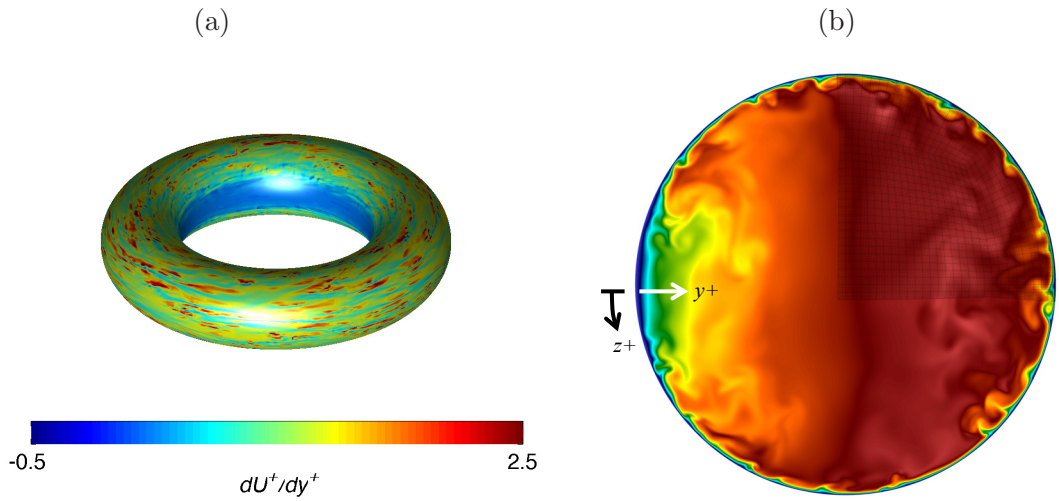


**Figure 1.** (a) Instantaneous inner-scaled streamwise wall-shear stress in the torus. (b) Cross-sectional view of an instantaneous streamwise velocity field, also showing one quarter of the in-plane spectral-element mesh. Note that the individual GLL poins within elements are also shown, and that in this panel dark blue and dark red correspond to $-0.1$ and 1.4, respectively. The coordinate system is defined as $x$, $y$ and $z$, which are the streamwise (into the page), wall-normal and azimuthal directions, respectively.

shear stress and in figure 1(b) a cross-sectional view of the torus is presented. The coordinate system is defined as $x$, $y$ and $z$, which are the streamwise, wall-normal and azimuthal directions, respectively. This is chosen to be consistent with the channel flow notation. The corresponding mean streamwise, wall-normal and azimuthal velocities are $U$, $V$ and $W$. We consider a bulk Reynolds number $Re_b = 2U_bR_p/\nu$ (based on bulk velocity $U_b$ and pipe diameter $2R_p$) of 19,000, which according to El Khoury *et al.* [50] yields a corresponding $Re_\tau = 550$ in straight pipes. As will be discussed below, due to the presence of the secondary flow induced by the pipe curvature, the value of $Re_\tau$ depends on the particular azimuthal location, and the averaged value is different from 550. The friction Reynolds number based on the averaged $u_\tau$ is $Re_\tau \approx 650$. Note that the Reynolds numbers are different between the torus and channel as shown in table 1. The geometry is completely defined with the curvature $\kappa = R_p/R_t$ (where $R_t$ denotes the radius of the torus, *i.e.*, the distance from the torus centre to the pipe centerline), which in the present study is set to 0.3. The computational mesh is designed for a straight pipe first [37, 50], following typical guidelines for DNS as discussed for instance in Ref. [39], and then this mesh is bent through analytical morphing in order to obtain the geometry of the toroidal pipe as discussed by Noorani *et al.* [37]. A total of 717,288 spectral elements with $N = 7$ was used to discretise the domain, which amounts to around 370 million grid points. The in-plane SEM mesh is shown in figure 1(b) and the simulation parameters are summarised in table 1. The simulations are run with constant mass flux, and periodicity is imposed in the streamwise direction. The laminar Poiseuille profile was used as initial condition, and low-amplitude pseudo-random noise was added to trigger transition to turbulence. After around 200 convective time units the turbulence could be considered fully-developed and independent of the initial conditions. Thus, the data under consideration in the present work was obtained after the initial 200 time units of simulation. Note that although Nek5000 solves the Navier–Stokes equations in a Cartesian frame of reference, rotation matrices were employed to express all the tensors in the local toroidal frame of reference as stated previously.

**Table 1.** Computational parameters for the toroidal pipe and the channel.

| | $Re_\tau$ | $L_x^+$ | $L_z^+$ | $\Delta_x^+$ | $\Delta_z^+$ | $N_x$ | $N_y$ | $N_z$ | $N_y \times N_z$ | $u_\tau \times 10^{-2}$ |
|---|---|---|---|---|---|---|---|---|---|---|
| Channel | 934 | 5870 | 2935 | 11.5 | 5.7 | 512 | 385 | 511 | - | 4.539 |
| Torus | 650 | 13614 | 4084 | [3.62, 11.81] | [1.71, 5.61] | 1936 | - | - | 189696 | 6.84 |

*2.3. Definition of back flow events*

The classification of back flow events is straightforward for the channel flow, where negative $\mathrm{d}U/\mathrm{d}y$ values correspond to back flow or reverse flow events. This is not the case for the flow through a toroidal pipe as shown in figure 2. Figures 2(a) and (b) show the instantaneous streamwise wall-shear stress for the torus and channel, respectively. It is clear that in the channel flow, the streamwise wall-shear stress profile exhibits an homogeneous pattern in the spanwise direction, whereas in the torus the distribution varies significantly from the inner bend ($z/\delta = 0$ and $2\pi$) to the outer bend ($z/\delta = \pi$) as shown in Ref. [51]. Note that in the context of the present work the variable $\delta$ denotes both the pipe radius $R_p$ in the torus and the channel half-height $h$. The probability density function of the orientation of the wall-shear stress vector is shown, in the form of a wind-rose plot, for the torus and the channel in figures 2(c,e) and (d,f), respectively. The wind rose plots essentially provide information of the magnitude and direction of the wall-shear stress vector. Figures 2(d) shows that the wall-shear stress vector in the channel is oriented predominantly in the streamwise direction, where the probability of the flow being aligned with the streamwise pressure gradient is approximately 12%. On the other hand, in the flow through the toroidal pipe the wall-shear stress vector exhibits three main preferential directions: the probability of the flow being aligned with the streamwise pressure gradient is around 5%, whereas the probability of it forming approximately $\pm 50^\circ$ with respect to it is around 4% on each of the two cases. Therefore, to determine the back flow events in a toroidal flow, the local wall-shear stress angle has to be considered using the streamwise and spanwise wall velocity gradients $\mathrm{d}U/\mathrm{d}y$ and $\mathrm{d}W/\mathrm{d}y$, respectively. Comparing the zoomed-in wind rose plots of the torus (figure 2e) and channel (figure 2f) clearly show that back flow events occur in both flows. The results also show a higher percentage of back flow events in the channel as compared to the torus. The temporal and streamwise average of the local wall-shear stress angle $\psi$ (in degrees) is shown in figure 3(a), using the same angular frame of reference as the one considered in figure 2. The angle $\psi$ at the inner and outer bends is $\psi = 90^\circ$, which implies that in these regions the wall-shear stress vector is aligned with the streamwise direction, and that there is no preferential direction for the spanwise wall-shear stress. The angle $\psi$ is continuously changing from the inner to the outer bend. However, our results clearly show that $\psi$ is symmetrical about either the inner or the outer bend. Since, as observed in figure 2(c), there are three preferential directions of the wall-shear stress, we will split the toroidal wall surface into several different regions to account for the variation in the local flow direction. To determine suitable regions to analyse back flow events, the rate of change of $\psi$ is chosen to discriminate the regions as shown in figure 3(b). The torus wall surface is split into six regions, which are denoted from R1 to R6. Note that R1, R2 and R3 are mirrored regions of R6, R5 and R4 respectively. Coincidently, this is similar to splitting the wall surface into four quadrants ($Q$) along the circumference in the cross section. Each quadrant has an arc length of $L_{arc} = \pi/2$. The four quadrant are: $Q1 =$ R1($0 < z/R_p < \pi/4$) + R6 ($7/4\pi < z/R_p < 2\pi$), $Q2 =$ R2 ($\pi/4 < z/R_p < 3/4\pi$), $Q3 =$ R5 ($5/4\pi < z/R_p < 7/4\pi$) and $Q4 =$ R3 ($3/4\pi < z/R_p < \pi$) + R4 ($\pi < z/R_p < 5/4\pi$).

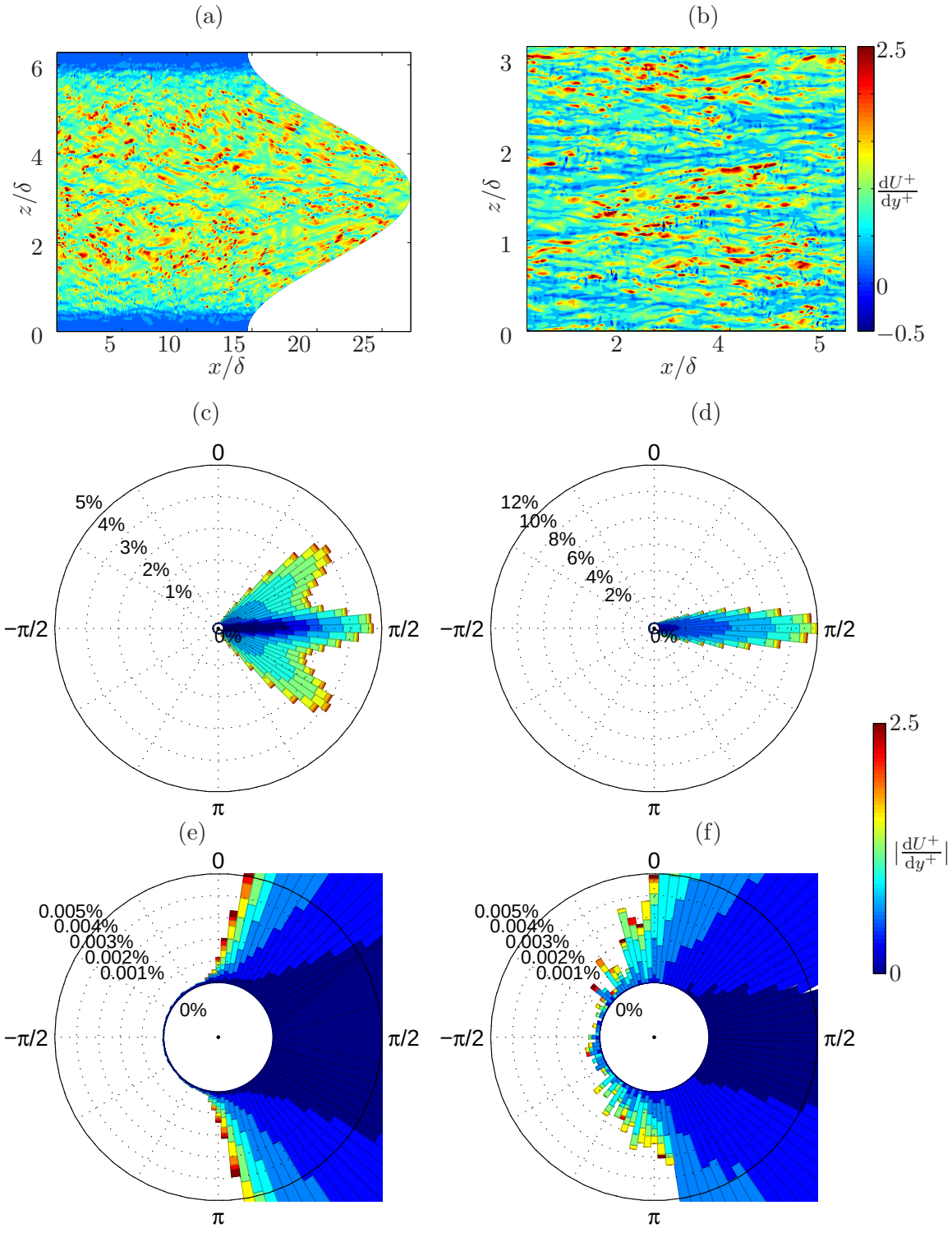


**Figure 2.** Instantaneous streamwise wall-shear stress for (a) torus (unwrapped) and (b) channel. Probability density function of the orientation of the wall-shear stress vector and magnitude for (c) torus with (e) zoomed-in view and for (d) channel with (f) zoomed-in view.

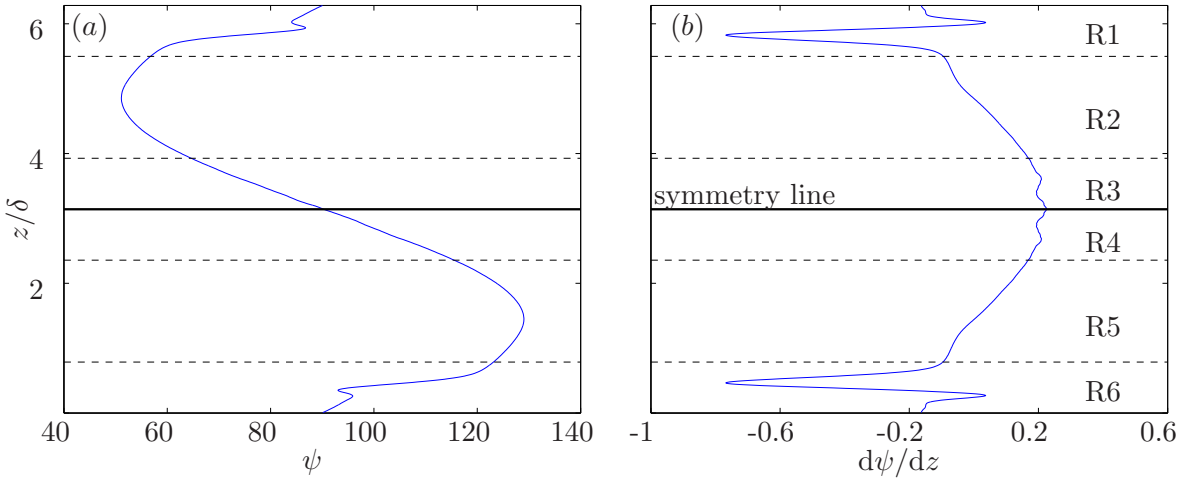


**Figure 3.** (a) Local average wall-shear stress angle $\psi$ (in degrees) for the torus. (b) Derivative of $\psi$ in the azimuthal direction. The solid line denotes the location of the outer bend. The dash lines split the torus into 6 regions, denoted R1 to R6, used for analysis purposes.

*2.4. Definition and characterisation of critical points*

To analyse the no-slip critical points on the wall, one can adopt a frame of reference in the channel flow, where the three orthogonal directions and velocities are labelled as $\mathbf{e}_1$, $\mathbf{e}_2$, $\mathbf{e}_3$ the three unit vectors along the three spatial coordinates. The velocity gradient tensor will be labelled as:

$$A_{ij} = \frac{\partial U_i}{\partial x_j}. \tag{1}$$

It can be shown that only $A_{12}$ and $A_{32}$ do not vanish due to the no-slip, impermeability and incompressibility conditions. Under these conditions, the three similarity invariants of $A_{ij}$ vanish: *i.e.* $P$, $Q$ and $R$ as defined by [52]. For a local flow characterisation, a higher-order truncation is required. We now introduce the no-slip tensor $\mathcal{A}_{ij}$ as:

$$\underline{\mathcal{A}} = \begin{bmatrix} \mathcal{A}_{11} & \mathcal{A}_{12} & \mathcal{A}_{13} \\ \mathcal{A}_{21} & \mathcal{A}_{22} & \mathcal{A}_{23} \\ \mathcal{A}_{31} & \mathcal{A}_{32} & \mathcal{A}_{33} \end{bmatrix} = \begin{bmatrix} \frac{\partial^2 U}{\partial x \partial y} & \frac{1}{2}\frac{\partial^2 U}{\partial y \partial y} & \frac{\partial^2 U}{\partial z \partial y} \\ \frac{\partial^2 V}{\partial x \partial y} & \frac{1}{2}\frac{\partial^2 V}{\partial y \partial y} & \frac{\partial^2 V}{\partial z \partial y} \\ \frac{\partial^2 W}{\partial x \partial y} & \frac{1}{2}\frac{\partial^2 W}{\partial y \partial y} & \frac{\partial^2 W}{\partial z \partial y} \end{bmatrix}. \tag{2}$$

Writing the Taylor expansion of the velocity field at a no-slip wall in matrix form leads to:

$$\begin{bmatrix} \mathring{x} \\ \mathring{y} \\ \mathring{z} \end{bmatrix} = \begin{bmatrix} 0 & A_{12} & 0 \\ 0 & 0 & 0 \\ 0 & A_{32} & 0 \end{bmatrix} + \begin{bmatrix} \mathcal{A}_{11} & \mathcal{A}_{12} & \mathcal{A}_{13} \\ \mathcal{A}_{21} & \mathcal{A}_{22} & \mathcal{A}_{23} \\ \mathcal{A}_{31} & \mathcal{A}_{32} & \mathcal{A}_{33} \end{bmatrix} \begin{bmatrix} x \\ y \\ z \end{bmatrix}, \tag{3}$$

or $\mathring{x}_i = A_{ij} + \mathcal{A}_{ij} x_j$ in more compact form. $\mathring{x}_i = \mathrm{d}x_i/\mathrm{d}\tau \neq \dot{x}_i = \mathrm{d}x_i/\mathrm{d}t$, and that incompressibility at a no-slip wall implies $\mathcal{A}_{21} = \mathcal{A}_{23} = 0$, $\mathcal{A}_{22} = -\left(\mathcal{A}_{11} + \mathcal{A}_{33}\right)/2$.
The two-dimensional skin-friction field at the wall is given as

$$\mathbf{s} = A_{12}\mathbf{e}_1 + A_{32}\mathbf{e}_3. \tag{4}$$

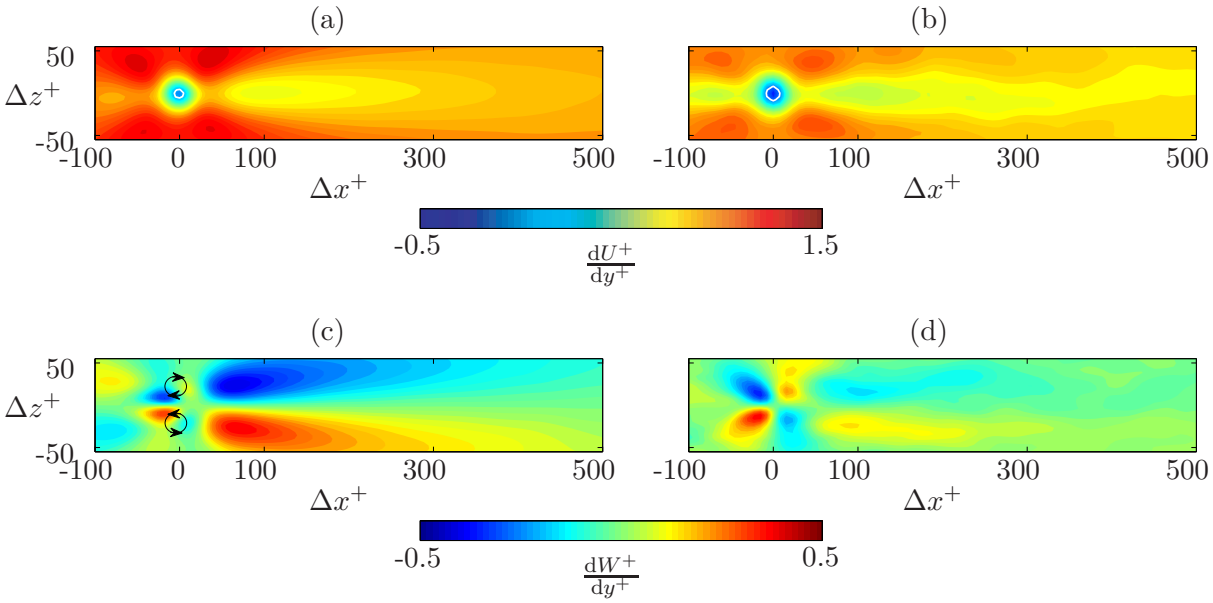


**Figure 4.** Distributions of $\mathrm{d}U^+/\mathrm{d}y^+$ (a & b) and $\mathrm{d}W^+/\mathrm{d}y^+$ (c & d) conditionally averaged to the presence of a back flow event at $\Delta x = \Delta y = 0$. The evaluation was performed over the entire azimuthal direction of the toroidal pipe. Left panels correspond to the torus and right panels to the channel. The white contour in panels (a) and (b) denote zero streamwise wall-shear stress.

The definition of critical points in $\mathbf{s}$ (see equation 4) and a description of how to locate them in a discrete numerical grid is similar to Ref. [30].

## 3. Results

The conditional averaging of $\mathrm{d}U^+/\mathrm{d}y^+$ and $\mathrm{d}W^+/\mathrm{d}y^+$ in the vicinity of a back flow event is first performed for the entire toroidal pipe without considering the local flow angle. The results are compared with the channel flow and are shown in figure 4. The top row, *i.e.* figures 4(a) and (b), show a comparison of the streamwise wall-shear stress $\mathrm{d}U^+/\mathrm{d}y^+$ in the torus and in the channel. Note that in these figures the centre of the back flow event is located at $\Delta x = \Delta z = 0$. The overall distribution is qualitatively similar in both cases, with low $\mathrm{d}U^+/\mathrm{d}y^+$ values right upstream and right downstream of the back flow event. The back flow events are flanked by regions of strong $\mathrm{d}U^+/\mathrm{d}y^+$ values, and interestingly the torus exhibits consistently larger shear-stress values in the vicinity of the back flow event than the channel. The mean diameter of these back flow events differs between the torus and the channel, with a mean diameter of about 16 viscous units in the torus and around 20 viscous units in the channel. Note that a diameter of around 20 viscous units was also reported by Vinuesa *et al.* [31] in the adverse-pressure-gradient turbulent boundary layer developing on the suction side of a wing section and by Lenaers *et al.* [16] in their channel flow simulations.

Figures 4(c) and (d) show the spanwise wall-shear stress distribution $\mathrm{d}W^+/\mathrm{d}y^+$ for the torus and the channel, respectively. In the case of the torus, the back flow event is flanked by two region of positive (negative) $\mathrm{d}W^+/\mathrm{d}y^+$, immediately followed by small areas of opposite sign in the downstream direction. This pattern suggests the presence of a pair of counter-rotating vortices in the vicinity of the back flow events, as illustrated in figure 4(c), which may be responsible for the formation of the region of reverse streamwise velocity.

In this region around the back flow event ($\Delta x^+ \approx [-50, 20]$, $\Delta z^+ \approx [-25, 25]$), this alternating pattern in $\mathrm{d}W^+/\mathrm{d}y^+$ is also present in the channel, although its topology is slightly different: the

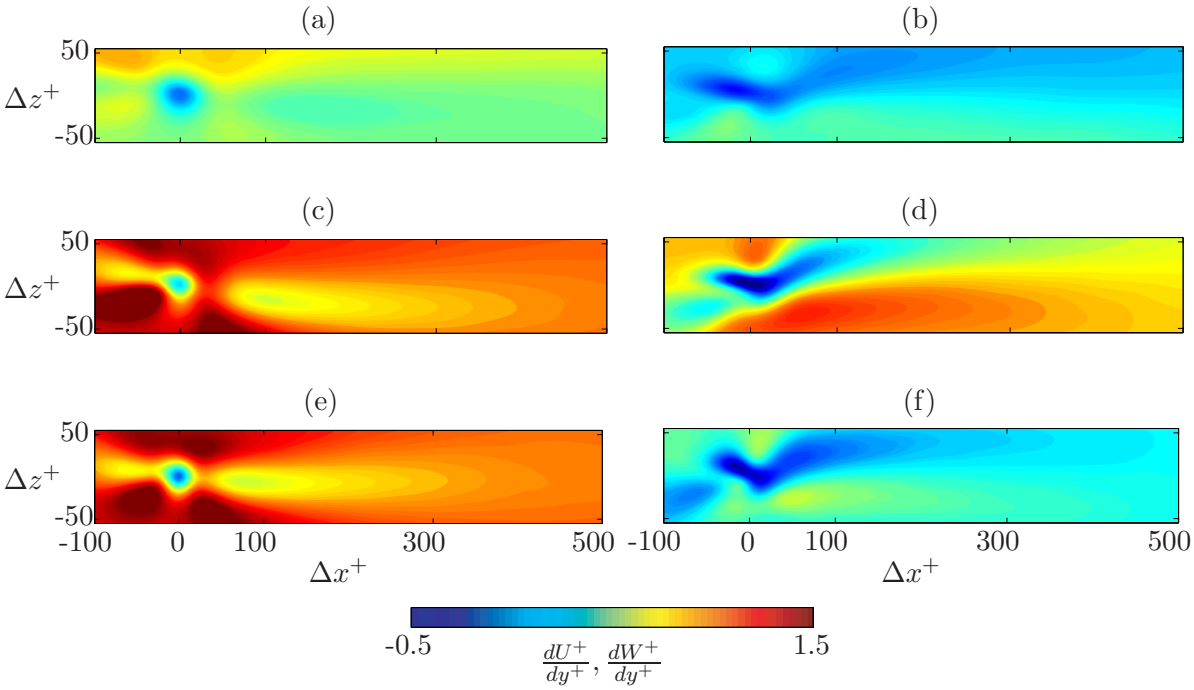


**Figure 5.** (Left panels) streamwise wall-shear stress $\mathrm{d}U^+/\mathrm{d}y^+$ and (right panels) spanwise wall-shear stress $\mathrm{d}W^+/\mathrm{d}y^+$. The results are shown for (a,b) region R1, (c,d) region R2 and (e,f) region R3. Regions are as defined in figure 3(b).

regions of positive (negative) spanwise wall-shear stress flanking the back flow event are larger, and are inclined in the streamwise direction, as opposed to what is observed in the torus. It is interesting to note that at further downstream distance ($\Delta x^+ > 50$) of the back flow event in the toroidal pipe, the $\mathrm{d}W^+/\mathrm{d}y^+$ signature is significantly stronger and longer than the upstream distribution, whereas the opposite is observed in the channel.

Since the results in figure 4 for the torus are a combination of contributions from the different

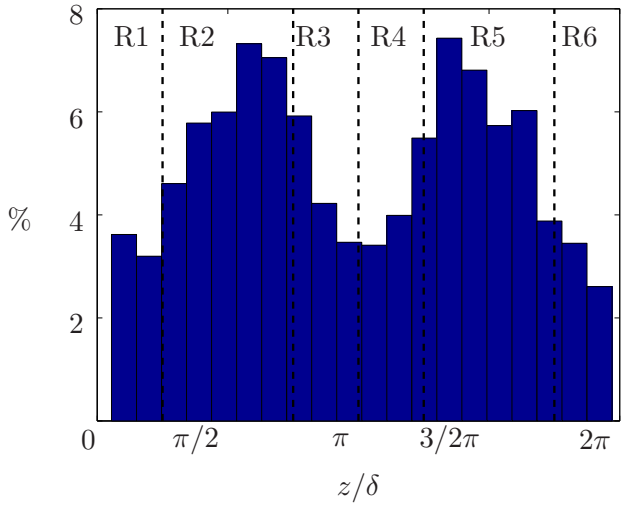


**Figure 6.** Histogram of back flow events in the toroidal pipe along the spanwise direction. R1 to R6 are the different regions as defined in figure 3.

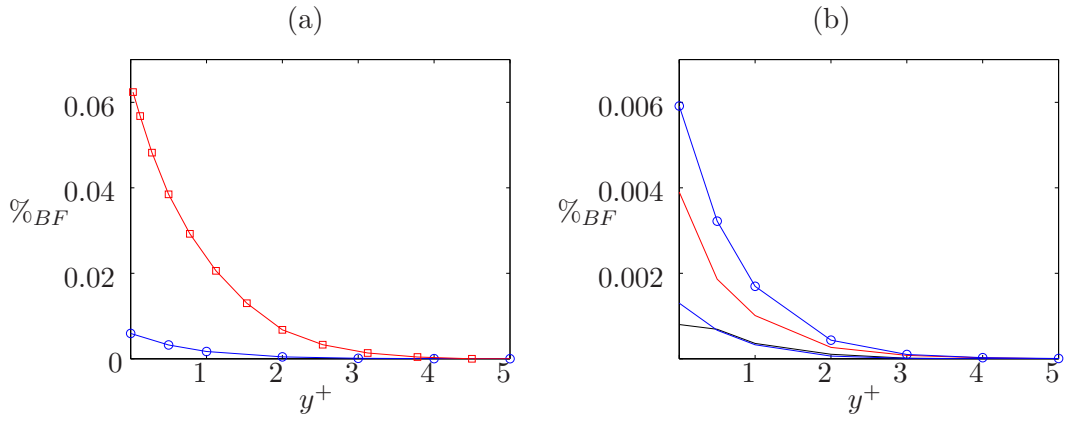


**Figure 7.** (a) Percentage of back flow events $\%_{BF}$ with increasing inner-scaled wall-normal distance for torus (blue line with ∘) and channel (red line with □). (b) Back flow events $\%_{BF}$ for torus decomposed into different regions. R1+R6 blue line; R2+R5 red line and R3+R4 black line. The blue line with dots is the same torus data as in (a).

regions defined in figure 3(b) (R1 to R6), it will be natural to investigate the influence of the secondary motion in the flow within the various areas of the torus. Since the regions are symmetrical about the symmetry line (see figure 3), only results from regions R1, R2 and R3 will be presented, which, however, include the contributions from their symmetrical counterparts to increase the sample space. The streamwise wall-shear stress $\mathrm{d}U^+/\mathrm{d}y^+$ from the torus is shown in figure 5(a, c, e) for regions R1, R2 and R3, respectively. This field exhibits significant differences in R1 compared to the field obtained when the contributions from all the regions are combined, as can be observed comparing figures 5(a) and 4(a). As documented by Noorani *et al.* [37], the pipe curvature induces an in-plane secondary flow which convects momentum from the inner to the outer bend through the core of the pipe, and from the outer back to the inner bend through the pipe walls. This secondary flow amounts to around 15% of the bulk velocity for the present curvature, which implies that it has a strong effect on the local flow features. The conditionally-averaged field in R1 reflects the fact that the strong vertical convection produces local laminar-like conditions in the inner bend. This results in a significantly weaker shear-stress field, with a small region of higher $\mathrm{d}U^+/\mathrm{d}y^+$ on one of the sides of the back flow event, induced by the secondary flow returning to the inner bend through the pipe wall. The distribution shown in figure 5(e) for region R3, *i.e.* for the outer bend, resembles the one in figure 4(a), although the latter exhibits smaller shear-stress values due to the fact that it also accounts for the weaker field present in the inner bend. Regarding region R2, the $\mathrm{d}U^+/\mathrm{d}y^+$ field shown in figure 5(c) shares some similarities with the outer bend, although its asymmetry is produced by the strong effect of the secondary flow in that region of the pipe. Figures 5(b, d, f) show the spanwise wall-shear stress $\mathrm{d}W^+/\mathrm{d}y^+$ for regions R1, R2 and R3, respectively. Here the profiles are clearly different from the ones obtained by considering the whole torus, which are shown in figure 4(c). This discrepancy is somewhat expected, since the secondary flow imprints a strong spanwise velocity *footprint* on the flow. The distributions for regions R1, R2 and R3 show a clear spanwise inclination, which is most prominent in figure 5(d), corresponding to region R2. Regions R1 and R3, *i.e.*, the inner and outer bend regions, are therefore slightly less influenced by the spanwise motion imposed by the secondary motion. Figure 6 shows the distribution of back flow events in the various regions (R1 to R6). Here the results further suggest that a strong spanwise secondary motion increases the occurrence of back flow events and in regions R1 and R3, the occurrence of back flow events decreases.

Next, a comparison of the percentage of back flow events ($\%_{BF}$) with increasing wall-normal

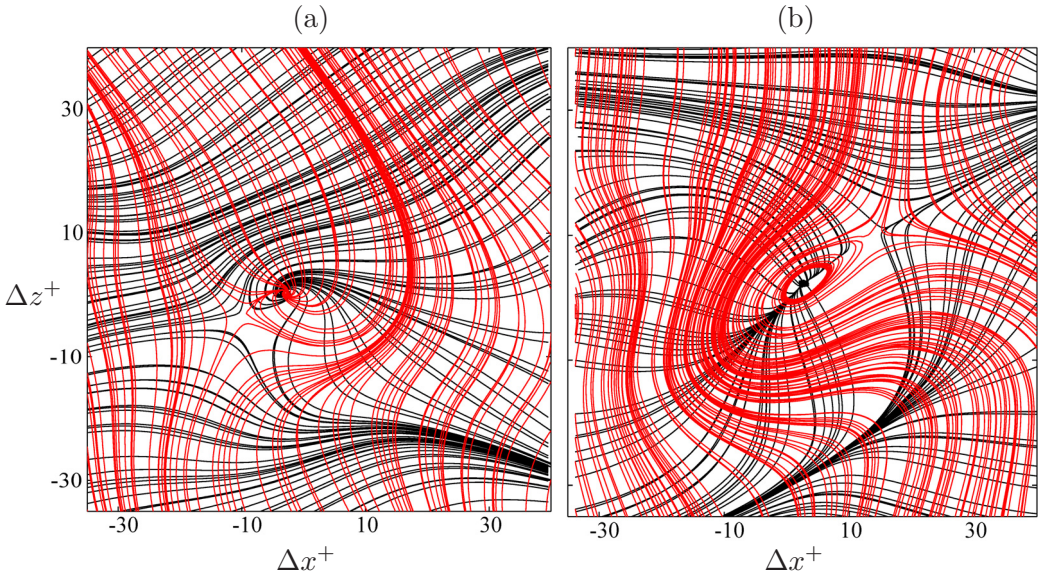


**Figure 8.** (Black) Skin-friction and (red) vorticity streamlines around the vicinity of a critical point for (a) torus and (b) channel. Note that the critical point is located at $\Delta x^+ = \Delta z^+ = 0$ in both cases.

distance $y^+$ is performed for the toroidal pipe and the channel flow, and is shown in figure 7. The percentage of back flow events decreases exponentially with increasing wall-normal distance, an observation in agreement with previously reported results by Lenaers *et al.* [16] and Vinuesa *et al.* [31]. Regarding the results from the torus, figure 7(a) shows that the percentage of back flow events is almost an order of magnitude lower than that of the channel flow. Moreover, the $\%_{BF}$ trend shows a similar exponential decay with $y^+$. A decomposition of the $\%_{BF}$ for the torus into different regions is shown in figure 7(b). For regions R1+R6 and R3+R4, which are least subjected to the influence of the secondary motion, they have very similar $\%_{BF}$ away from the wall. The $\%_{BF}$ for region R2+R5 is consistently larger than in the other regions. The results here suggest that the vortical structures required for the production of back flow events are significantly affected by the secondary flow in the toroidal pipe. Further inspection of figures 4(c) and (d) indicates that the spanwise wall-shear stress pattern responsible for the pair of counter-rotating vortices is weaker in the torus, a fact that is connected with the lower occurrence of reverse flow events. As reported in Ref. [31], APG TBLs exhibit higher occurrence of back flow events than ZPGs at the same Reynolds number. This is due to the fact that the wall-normal convection produced by the APG reduces the near-wall velocity, thus promoting the formation of regions of negative velocity. In the case under study here, the strong secondary flow convects momentum from the inner to the outer bend of the pipe, therefore the flow on the outer bend experiences a strong convection towards the wall, with the opposite effect to that of an APG, thus resulting in a reduction of back flow events. As reported by Lenaers *et al.* [16], back flow events are absent in laminar flows, and are only produced as extreme events in turbulent flows. The very strong convection away from the inner bend produces laminar-like conditions, as can be observed for instance in figure 1(b), therefore justifying the reduction of back flow events in this region. Overall, the present results suggest that the percentage of back flow events drops to around zero for wall-normal locations above $y^+ = 5$.

Figures 8(a) and (b) show the flow field around the vicinity of critical points for the torus and the channel, respectively. It has been shown that critical points exist in pairs and in close proximity to each other [29]. This pair of critical points consists of one node and one saddle. The critical points (nodes) for both flows are located at $\Delta x^+ = \Delta z^+ = 0$. The saddle for the

**Table 2.** Summary of back flow and critical point statistics in toroidal pipe and channel flow.

| | **Torus** | **Channel** |
|---|---|---|
| Percentage area of back flow (at the wall) | 0.006% | 0.06% |
| Percentage area of back flow for R1+R6 (at the wall) | 0.0008% | - |
| Percentage area of back flow for R2+R5 (at the wall) | 0.0039% | - |
| Percentage area of back flow for R3+R4 (at the wall) | 0.0013% | - |
| Number of back flow events (per $10^6$ viscous unit area) | 0.3 | 1.8 |
| Mean diameter of back flow event (in viscous units) | 16 | 20 |
| Number of critical points (per $10^6$ viscous unit area) | 0.35 | 2 |
| Number of critical points for R1+R6 (per $10^6$ viscous unit area) | 0.144 | - |
| Number of critical points for R2+R5 (per $10^6$ viscous unit area) | 0.136 | - |
| Number of critical points for R3+R4 (per $10^6$ viscous unit area) | 0.07 | - |

torus is at $\Delta x^+, \Delta z^+ \approx (-10, -5)$ and for the channel is at $\Delta x^+, \Delta z^+ \approx (15, 10)$. From figure 8, both flow fields show similar skin-friction streamlines and skin-friction vorticity lines patterns. Even though both flows are very different in nature, the results here suggest that critical point characteristics are similar at the wall and might be an essential component in the dynamics of wall-bounded turbulent flows.

A summary of the statistics for the back flow events and critical points in the toroidal pipe and in the channel is presented in table 2. The toroidal pipe consistently shows a lower occurrence of back flow events and critical points (both in terms of percentage area of the wall and number of events per $10^6$ viscous unit area) when compared to the channel flow. These statistics also show that the number of back flow events is lower than the number of critical points in the two flow cases under study. The further decomposition of the torus statistics ($\%_{BF}$ and number of critical points at the wall) into the three main regions are also shown in table 2. Results clearly indicated higher occurrence of back flow events and critical points where secondary motion is strongest.

## 4. Conclusions

A DNS of the turbulent flow through a toroidal pipe at $Re_\tau \simeq 650$ was performed, using the spectral-element code Nek5000 [47], with the aim of analysing the characteristics of the wall-shear stress vector. Back flow events, *i.e.* regions of reverse flow, were characterised in the torus and compared with the ones obtained in a DNS of turbulent channel flow at $Re_\tau \simeq 934$. Our results show that back flow events are less numerous in the toroidal pipe than in the channel, with probabilities of occurrence of 0.006% and 0.06% in both cases, respectively. The fields of streamwise and spanwise wall-shear stress conditioned to the presence of a back flow event are stronger in the torus, and the diameter of the reverse flow regions is smaller than in the channel. The diameter is around 16 viscous units in the former, while its value is about 20 in the channel, in agreement with the results reported in other channel flow simulations [16] and in APG TBLs [31]. Note that, although the two flows are compared at different Reynolds numbers, the $Re$ effect is much weaker than the discrepancy observed in the two cases, as reported in Ref. [16]. These differences are therefore explained by the effect of the secondary flow present in the torus, which convects momentum from the inner to the outer bend through the core of the pipe, and back from the outer to the inner bend through the pipe walls. This secondary flow, which amounts to around 15% of the bulk velocity [37] for the present curvature, inhibits the formation of back flow events in the outer bend through a mechanism opposite to the one reported in APG TBLs

[31]. On the other hand, the significant wall-normal convection from the inner bend produces laminar-like conditions, which also lead to a dramatic reduction in the emergence of reverse-flow regions [16]. It is important to note that although it is common to impose periodicity in the streamwise and spanwise directions in turbulent channel flow simulations, in the torus the flow is naturally streamwise-periodic. Therefore, the present results provide clear evidence that back flow events and critical points are genuine features and not artifacts of specific boundary or inflow conditions in simulations and/or measurement uncertainties in experiments. Future extensions of the present study will utilise the entire flow field of the toroidal pipe to investigate flow structures above these back flow events and critical points. Another interesting possible extension of this study would be to analyse and compare the impact of the secondary flow in turbulent ducts on back flow events and critical points.

## Acknowledgments

This work was supported with supercomputing resources provided by the Phoenix HPC service at the University of Adelaide. Computer time was provided by the Swedish National Infrastructure for Computing (SNIC). This study was funded in part by the Coturb Grant (grant number ERC-2014.AdG-669505) of the European Research Council. RV, RÖ and PS acknowledge the funding provided by the Swedish Research Council (VR) and the Knut and Alice Wallenberg Foundation. MSC and CC acknowledge the financial support of the Australian Research Council. We are grateful to A. Ianiro for his thoughtful review of this manuscript.

## References

[1] Mathis R, Hutchins N and Marusic I 2009 *J. Fluid Mech.* **628** 311–337
[2] Schlatter P and Örlü R 2010 *Phys. Fluids* **22** 051704
[3] Marusic I, Mathis R and Hutchins N 2010 *Science* **329** 193–196
[4] Vinuesa R, Hites M H, Wark C E and Nagib H M 2015 *Phys. Fluids* **27** 105107
[5] Klewicki J, Chin C, Blackburn H M, Ooi A and Marusic I 2012 *Phys. Fluids* **24** 045107
[6] Poon E K, Hayat U, Thondapu V, Ooi A, Asrar Ul Haq M, Moore S, Foin N, Tu S, Chin C, Monty J P, Marusic I and Barlis P 2015 *Coron. Artery Dis.* **26** e43–e54
[7] Arzani A, Gambaruto A M, Chen G and Shadden S C 2016 *J. Fluid Mech.* **790** 158–172
[8] Dairay T, Fortuneé V, Lamballais E and Brizzi L E 2015 *J. Fluid Mech.* **764** 362–394
[9] Wu Z, Laurence D, Iacovides H and Afgan I 2017 *Int. J. Heat Mass Transf.* **110** 193–208
[10] Vinuesa R, Hosseini S M, Hanifi A, Henningson D S and Schlatter P 2017 *Flow Turbul. Combust.* **99** 613–541
[11] Negi P S, Vinuesa R, Schlatter P, Hanifi A and Henningson D S 2017 *In Proc. TSFP-10* 1D–3
[12] Carlomagno G and Ianiro A 2014 *Exp. Therm. Fluid Sci.* **58** 15–35
[13] Surana A, Grunberg O and Haller G 2006 *J. Fluid Mech.* **564** 57–103
[14] Alam M R, Liu W and Hallerb G 2006 *Phys. Fluids* **18** 043601
[15] Brunton S L, Rowley C W and Williams D R 2013 *J. Fluid Mech.* **724** 203–233
[16] Lenaers P, Li Q, Brethouwer G, Schlatter P and Örlü R 2012 *Phys. Fluids* **24** 035110
[17] Yao Y C, Huang W X and Xu C X 2017 *Acta Mech. Sin.* DOI 10.1007/s10409-017-0687-2
[18] Johansson G 1988 *An experimental study of the structure of a flat plate turbulent boundary layer, using laser-Doppler velocimetry* Ph.D. thesis Chalmers U. Technology
[19] Spalart P R and Coleman G N 1997 *Eur. J. Mech. B* **16** 169–189
[20] Hu Z W, Morfey C L and Sandham N D 2006 *AIAA J.* **44** 1541–1549
[21] Eckelmann H 1974 *J. Fluid Mech.* **65** 439–459
[22] Colella K J and Keith W L 2003 *Exp. Fluids* **34** 253–260
[23] Willert C E, Cuvier C, Foucaut J M, Klinner J, Stanislas M, Laval J P, Srinath S, Soria J, Amili O, Atkinson C, Kahler C J, Scharnowski S, Hain R, Schröder A, Geisler R, Agocs J and Röse A 2018 *Exp. Therm. Fluid Sci.* **91** 320–328
[24] Brücker C 2015 *Phys. Fluids* **27** 031705
[25] Brücker C, Bauer D and Chaves H 2007 *Exp. Fluids* **42** 737–749
[26] Große S and Schröder W 2008 *Meas. Sci. Technol.* **19** 015403
[27] Vinuesa R and Örlü R 2017 *Experimental Aerodynamics* ed Discetti S and Ianiro A (CRC Press) chap 12
[28] Monty J, Chin C, Chong M and Marusic I 2012 *In Proc. ERCOFTAC ETMM-9*
[29] Chong M S, Monty J P, Chin C and Marusic I 2012 *J. Turbul.* **13** 1–10

[30] Cardesa J I, Monty J P, Soria J and Chong M S 2014 *J. Phys.: Conf. Ser.* **506** 012009
[31] Vinuesa R, Örlü R and Schlatter P 2017 *J. Turbul.* **18** 170–185
[32] Bobke A, Vinuesa R, Örlü R and Schlatter P 2017 *J. Fluid Mech.* **820** 667–692
[33] Bross M and Kähler C J 2017 *In Proc. TSFP-10* 7A–5
[34] Kühnen J, Holzner M, Hof B and Kuhlmann H 2014 *J. Fluid Mech.* **738** 463–491
[35] Canton J, Schlatter P and Örlü R 2016 *J. Fluid Mech.* **792** 894–909
[36] Canton J, Örlü R and Schlatter P 2017 *Int. J. Heat Fluid Flow* **66** 95–107
[37] Noorani A, El Khoury G K and Schlatter P 2013 *Int. J. Heat Fluid Flow* **41** 16–26
[38] Noorani A and Schlatter P 2016 *Int. J. Heat Fluid Flow* **61** 108–116
[39] Chin C 2011 *Numerical study of internal wall-bounded turbulent flows* Ph.D. thesis University of Melbourne
[40] Chin C, Philip J, Klewicki J, Ooi A and Marusic I 2014 *J. Fluid Mech.* **757** 747–769
[41] Kalpakli Vester A, Örlü R and Alfredsson P H 2016 *Appl. Mech. Rev.* **68** 050802
[42] Kim J, Moin P and Moser R 1987 *J. Fluid Mech.* **177** 133–166
[43] del Álamo J, Jiménez J, Zandonade P and Moser R D 2006 *J. Fluid Mech.* **561** 329–358
[44] Saha S, Chin C, Blackburn H and Ooi A 2011 *Int. J. Heat Fluid Flow* **32** 1083–1097
[45] Chin C, Ooi A S H, Marusic I and Blackburn H M 2010 *Phys. Fluids* **22** 115107
[46] Chin C, Monty J P and Ooi A 2014 *Int. J. Heat Fluid Flow* **45** 33–40
[47] Fischer P F, Lottes J W and Kerkemeier S G 2008 NEK5000: Open source spectral element CFD solver. Available at: `http://nek5000.mcs.anl.gov` Tech. rep. Argonne NL
[48] Patera A T 1984 *J. Comput. Phys.* **54** 468–488
[49] Fischer P and Mullen J 2001 *C. R. Acad. Sci. Paris* **332** 265–270
[50] El Khoury G, Schlatter P, Noorani A, Fischer P, Brethouwer G and Johansson A 2013 *Flow Turbul. Combust.* **91** 475–495
[51] Noorani A, Sardina G, Brandt L and Schlatter P 2016 *J. Fluid Mech.* **793** 248–279
[52] Chong M, Perry A and Cantwell B 1990 *Phys. Fluids* **2** 765–777